

WEST Physics Basis

C. Bourdelle¹, J.F. Artaud¹, V. Basiuk¹, M. Bécoulet¹, S. Brémond¹, J. Bucalossi¹, H. Bufferand¹, G. Ciraolo¹, L. Colas¹, Y. Corre¹, X. Courtois¹, J. Decker², L. Delpech¹, P. Devynck¹, G. Dif-Pradalier¹, R.P. Doerner³, D. Douai¹, R. Dumont¹, A. Ekedahl¹, N. Fedorczak¹, C. Fenzi¹, M. Firdaouss¹, J. Garcia¹, P. Ghendrih¹, C. Gil¹, G. Giruzzi¹, M. Goniche¹, C. Grisolia¹, A. Grosman¹, D. Guilhem¹, R. Guirlet¹, J. Gunn¹, P. Hennequin⁴, J. Hillairet¹, T. Hoang¹, F. Imbeaux¹, I. Ivanova-Stanik⁵, E. Joffrin¹, A. Kallenbach⁶, J. Linke⁷, T. Loarer¹, P. Lotte¹, P. Maget¹, Y. Marandet⁸, M.L. Mayoral^{9,10}, O. Meyer¹, M. Missirlian¹, P. Mollard¹, P. Monier-Garbet¹, P. Moreau¹, E. Nardon¹, B. Pégourié¹, Y. Peysson¹, R. Sabot¹, F. Saint-Laurent¹, M. Schneider¹, J.M. Travère¹, E. Titrone¹, S. Vartanian¹, L. Vermare⁴, M. Yoshida¹¹, R. Zagorski⁵ and JET Contributors^a

¹ CEA, IRFM, F-13108 Saint-Paul-lez-Durance, France

² Centre de Recherches en Physique des Plasmas, Ecole Polytechnique Fédérale de Lausanne, Switzerland

³ Center for Energy Research, University of California in San Diego, La Jolla, CA 92093-0417, USA

⁴ Ecole Polytechnique, LPP, CNRS UMR 7648, 91128 Palaiseau, France

⁵ Institute of Plasma Physics and Laser Microfusion, Warsaw, Poland

⁶ Max Planck Institute f. Plasma Physics, Boltzmannstr 2, D-85748 Garching, Germany

⁷ Forschungszentrum Jülich, D-52425 Jülich, Germany

⁸ Aix-Marseille Université, CNRS, PIIM, UMR 7345, 13013 Marseille, France

⁹ CCFE, Culham Science Centre, Abingdon, Oxon, OX14 3DB, UK

¹⁰ EUROfusion Programme Management Unit, D-85748 Garching, Germany

¹¹ Japan Atom Energy Agency, Naka, Ibaraki, Japan

E-mail: clarisse.bourdelle@cea.fr

Received 17 December 2014, revised 24 March 2015

Accepted for publication 7 April 2015

Published 6 May 2015



CrossMark

Abstract


With WEST (Tungsten Environment in Steady State Tokamak) (Bucalossi *et al* 2014 *Fusion Eng. Des.* **89** 907–12), the Tore Supra facility and team expertise (Dumont *et al* 2014 *Plasma Phys. Control. Fusion* **56** 075020) is used to pave the way towards ITER divertor procurement and operation. It consists in implementing a divertor configuration and installing ITER-like actively cooled tungsten monoblocks in the Tore Supra tokamak, taking full benefit of its unique long-pulse capability. WEST is a user facility platform, open to all ITER partners. This paper describes the physics basis of WEST: the estimated heat flux on the divertor target, the planned heating schemes, the expected behaviour of the L–H threshold and of the pedestal and the potential W sources. A series of operating scenarios has been modelled, showing that ITER-relevant heat fluxes on the divertor can be achieved in WEST long pulse H-mode plasmas.

Keywords: plasma facing components, divertor, tokamak, plasma physics

(Some figures may appear in colour only in the online journal)

1. Introduction

Power exhaust is one of the main challenges for next step fusion devices [1]. In ITER and DEMO, the plasma facing

 Content from this work may be used under the terms of the Creative Commons Attribution 3.0 licence. Any further distribution of this work must maintain attribution to the author(s) and the title of the work, journal citation and DOI.

^a See the appendix of Romanelli F. *et al* 2014 *Proc. 25th IAEA Fusion Energy Conf. 2014 (Saint Petersburg, Russia)* <http://iopscience.iop.org/0029-5515/55/10/104001>.

components (PFCs) will experience extreme heat and particle loads as well as unprecedented levels of cumulated particle fluence and gigajoules of energy to be extracted in a single discharge. WEST provides an integrated platform for testing the ITER divertor components under combined heat and particle loads in a tokamak environment [2]. It will allow assessing the power handling capabilities and the lifetime of ITER high heat flux tungsten divertor technology under ITER-relevant power loads (10–20 MW m⁻²), particle fluence (~10²⁷ D m⁻²) and time scales (above 100 s). Operation in WEST will also allow validating a scheme for the protection

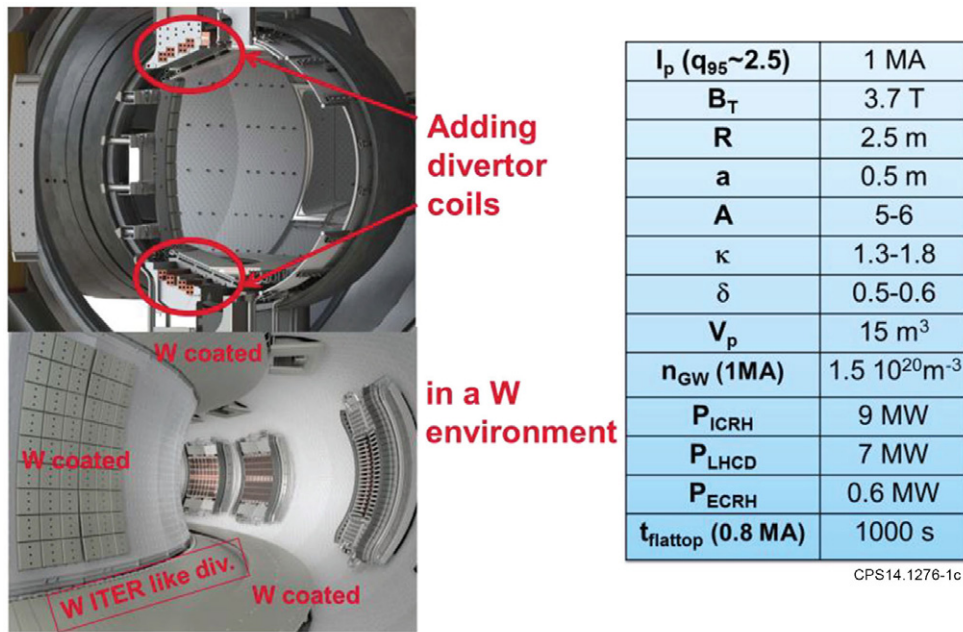


Figure 1. CAD views of WEST and a table summarizing the WEST main parameters.

of actively cooled metallic PFCs. The WEST research plan has been structured around two main topical headlines: ‘ITER grade PFC tests’ and ‘towards long pulse H-mode and steady-state operation’. The research plan is evolving with the project and revised with the WEST partners on a yearly basis. Such interactions with the fusion community have started during the 1st WEST International Workshop that took place in Aix-en-Provence in 2014 [3].

In order to fulfil its scientific objectives, WEST is equipped with upper and lower divertor coils, W coated upper divertor, baffle, inner bumper and with a flexible lower divertor made of twelve 30° sectors where the ITER-like W monoblocks will be installed [4]. The additional heating and current drive power is provided by high frequency heating systems, namely ion cyclotron resonance heating (ICRH) and lower hybrid current drive (LHCD), delivering up to 9 MW of ICRH power and 7 MW of LHCD power. See figure 1 for CAD views of WEST and for a table summarizing the main plasma and heating system parameters (maximum values).

To address the programme headlines, three groups of standard scenarios have been targeted. Scenarios at medium power (12 MW) are needed for testing the ITER grade PFC and demonstrating integrated H-mode long pulse operation (~60 s) while ensuring relevant heat fluxes on the divertor (in the range 10–20 MW m⁻²). To study plasma wall interactions at high particle fluence, scenarios up to 1000 s at 10 MW are foreseen. Finally, high power scenarios at 15 MW are developed for 30 s high performance discharges. In the WEST actively cooled environment, there is no hard technological limit on the pulse duration, 1000 s is an indicative time scale.

To prepare these scenarios, the amount of additional power required to achieve 10–20 MW m⁻² is discussed in section 2; ICRH and LHCD modelling is presented in section 3; the fuelling and pumping capacities are detailed in section 4; the estimated L–H power threshold, pedestal and ELMs are studied in section 5; the expected density profile is reviewed

in section 6; in section 7, W sources are discussed and finally in section 8 integrated modelling of four WEST scenarios are presented before concluding in section 9.

2. Expected heat flux on the divertor target

The peak heat flux is constrained by geometrical factors, magnetic equilibrium (flux expansion) and by the SOL physics.

The WEST magnetic configurations allow for elongated plasmas in lower or upper single null, or double null configurations. For a standard elongated lower single null case, the X-point height range, at for example 0.7 MA, is up to 10 cm, see figure 2. The equilibria of figure 2 are used as references equilibria in the rest of the scenario study presented here. They are constrained by a fixed toroidal magnetic field $B_T = 3.7$ T at 2.5 m and by an external radius of 2.93 m which is compatible with ICRH and LHCD launchers positions. It is to note that ICRH and LHCD launchers can be moved radially between or during shots, for ICRH between 2.89 and 3.06 cm and for LHCD from 2.91 and up to 3.06 cm. All equilibria are computed with the free boundary equilibrium code CEDRES++ [5].

The pulse duration is constrained by the maximum current flowing in the actively cooled copper divertor coils. Steady state is reached with a total current in the divertor coils of 200 kA.turn. For shorter pulses of 15 s, up to 320 kA.turn can be reached, limited by the coils power supplies capabilities (20 kA). The link between the X-point height and the plasma current, I_p , is illustrated in figure 3, for the two divertor currents 200 and 320 kA.turn. In steady state, up to $I_p = 0.8$ MA can be reached and X-point height of 12 cm corresponds to $I_p = 400$ kA while $I_p = 1$ MA is achievable with a q_{95} of 2.5, for an X-point height of 1 cm for this kind of equilibria.

In WEST the angle of incidence of the magnetic field lines on the lower divertor is toroidally modulated by magnetic

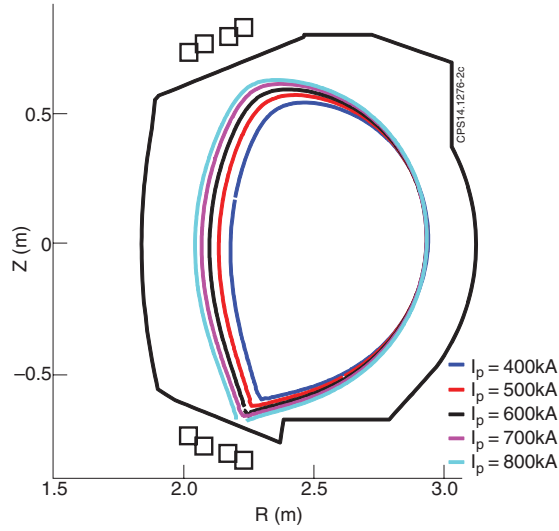


Figure 2. CEDRES++ free boundary set of equilibria for $B_T = 3.7$ T (at 2.5 m); with a fixed external radius of 2.93 m and with the steady-state divertor coil current of 200 kA.turn.

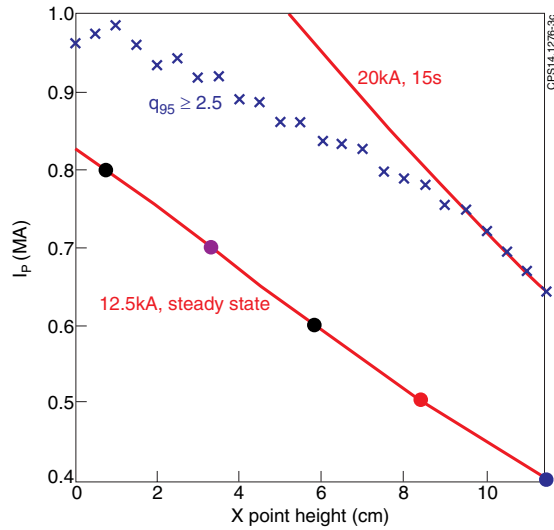


Figure 3. At fixed $B_T = 3.7$ T, range of accessible I_p and X-point heights corresponding to the references equilibria illustrated by figure 2. The limits due to the divertor coils are in red, one for the steady state and one corresponding to the maximal divertor coils current. In blue is the limit corresponding to $q_{95} = 2.5$.

field ripple due to 18 superconducting toroidal field coils. The magnetic ripple is about 2% at the last closed flux surface in WEST. The angle and its modulation are illustrated for an X-point height of 3 cm by a top view of 20° of the lower divertor in figure 4. The grazing angle of incidence close to the strike points for this configuration is between 2° and 3°, i.e. in the ITER range.

The WEST heat flux fall-off length λ_q in H-mode is extrapolated from the scaling law published in [6]:

$$\lambda_q = (0.73 \pm 0.38) \times B_T^{-0.78 \pm 0.25} q_{\text{cyl}}^{1.2 \pm 0.27} P_{\text{SOL}}^{0.10 \pm 0.11}. \quad (1)$$

With B_T the toroidal magnetic field, P_{SOL} , the power flowing through the last closed flux surface in the SOL and q_{cyl} the cylindrical safety factor.

For WEST, $B_T = 3.7$ T and P_{SOL} is iterated to match a peak heat flux on the divertor of 10 MW m^{-2} . The iteration is

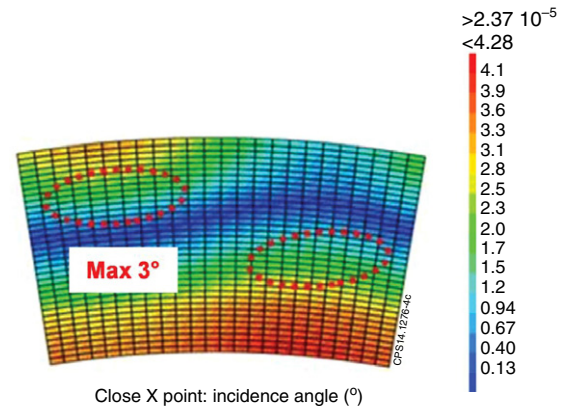


Figure 4. Top view of a 30° divertor sector. The low field side is at the top of the figure and the high field side at the bottom. Angle of incidence of the field lines in ° for the low X-point configuration. The high heat flux area is circled in red.

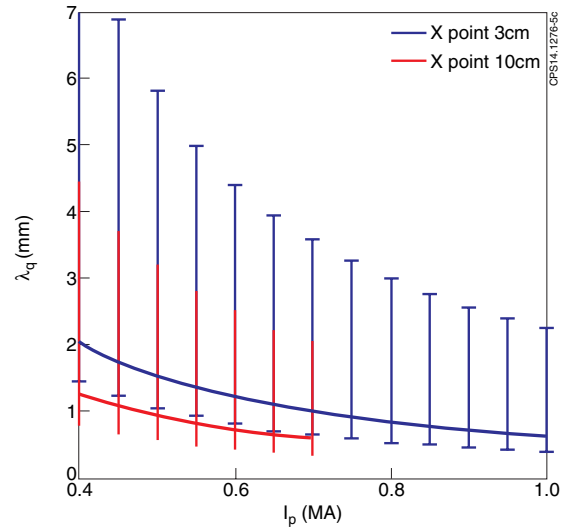


Figure 5. Heat flux fall-off length λ_q in H mode based on the scaling law from [6], for an X-point height of 3 cm in red and an X-point height of 10 cm in blue. The error bars represent the uncertainties on the exponents of equation (1).

done starting with a λ_q independent of P_{SOL} used to determine the wetted area which constrain the power on the divertor, P_{div} . P_{div} is assumed to be 80% of P_{SOL} . The obtained value of P_{SOL} is then used to determine λ_q using equation (1). One finally finds λ_q as a function of I_p as illustrated by figure 5. The error bars correspond to the extremes of equation (1) taken as follows: extreme of the prefactor and the extreme of one of the two exponents on B_T or q_{cyl} . Since the constraint on P_{SOL} is a peak heat flux of 10 MW m^{-2} , the range of expected values for λ_q varies with the X point heights. Two heights, 3 and 10 cm, are illustrated in figure 5. The range of expected λ_q based on the scaling law proposed in [6] is rather large and varies from 0.5 to 7 mm.

The amount of additional power to reach a peak heat flux of 10 MW m^{-2} is estimated with the following assumptions: 40% of the additional power is supposed to be radiated before reaching the divertor; an asymmetry low field side versus high field side with 2/3 of the power on the LFS is supposed; a spreading factor, S , is taken such that: $S = 0.4 \times \lambda_q$ and the

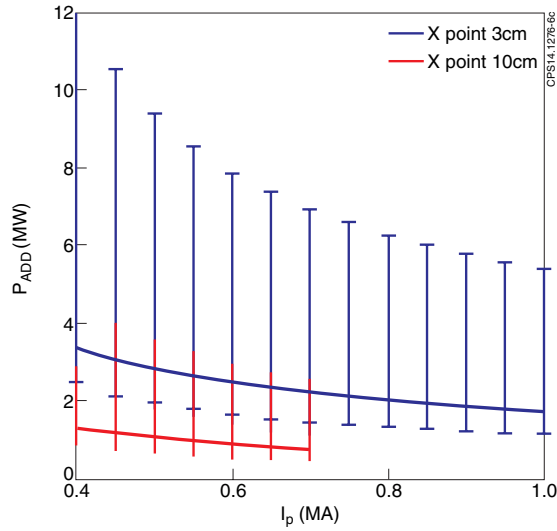


Figure 6. Additional power required to reach 10 MW m^{-2} on the WEST divertor. Using the scaling law of [6], accounting for the magnetic ripple and for an X-point height of 3 cm in red and an X-point height of 10 cm in blue.

uncertainties on λ_q illustrated in figure 5 are accounted for. The additional power required to reach 10 MW m^{-2} is plotted versus I_p in figure 6 for two X-point heights (3 and 10 cm). For 3 cm, the flux expansion factor is 9, whereas at a higher X-point it is down to 3, leading to higher peak heat fluxes for an identical amount of power reaching the divertor region.

10 MW m^{-2} can be achieved onto the divertor with an additional power varying greatly from less than 2 MW to up to more than 10 MW [7]. Given the large uncertainties, the flexibility provided in WEST through a large range of X-point heights is a key feature. The large error bars are essentially due to the uncertainties on the expected λ_q . This points towards the importance of the heat flux fall-off length studies in progress on various machines. Such studies will be carried out, thanks to a unique IR coverage of the divertor region [8], adding information on the large aspect ratio impact on SOL transport. Overall, in WEST, the level of additional power is sufficient to achieve the nominal ITER steady-state heat flux of 10 MW m^{-2} , and up to 20 MW m^{-2} , corresponding to slow transient heat fluxes for ITER.

In addition to the steady-state heat flux discussed above, transient heat loads due to ELMs and disruptions are also to be taken into account. For ITER, these heat loads are a serious issue for PFCs, which requires mitigation [1].

For WEST, ELMs are expected to be benign, significantly below the tungsten melting threshold (see section 5 for more details), and do not require specific mitigation. Dedicated campaigns will be run to assess the impact of a large number of such sub-damage threshold ELMs on tungsten components ageing, taking advantage of the long pulse capability of Tore Supra. Indeed, it has been shown that exposure to a large number of thermal transients or high deuterium and/or helium particle fluence can lower the damage threshold of the component, induce cracks development within the material, degrade its thermal conductivity, eventually leading to enhanced erosion [9–11]. In particular, the tungsten PFC damage threshold has been observed to decrease with the

number of ELM like cycles in e-beam testing facilities [9]. WEST will allow complementing these results under plasma exposure in a tokamak environment.

As far as disruptions are concerned, the heat loads for WEST are estimated to be comparable to those of Tore Supra in its previous configuration [12], and should not induce serious damage to the PFCs. On the other hand, runaway electrons could be an issue. However, elongated plasmas have been shown to be less prone to runaway production than circular plasmas. Should WEST disruptions require mitigation (in particular due to runaways production or severe fast vertical displacement events), WEST is equipped with a massive gas injection system (see also section 4).

3. High frequency plasma heating

As presented in the introduction, WEST plasmas will be heated by a combination of LHCD power, up to 7 MW, and ICRH power, up to 9 MW. It is essential to adapt the heating systems to the WEST configuration, and also to verify the adequacy of these heating schemes with H-mode operation in terms of power coupling, fast particle confinement and ELM resilience in a metallic environment. It will complement active efforts carried out in metallic environments on JET-ILW [13], ASDEX Upgrade [14, 15], Alcator C-Mod [16] and FTU [17].

3.1. Lower hybrid current drive

The LHCD system for WEST consists of two fully actively cooled multijunction launchers, the so-called passive active multijunction (PAM) [18] and the fully active multijunction (FAM) [19], where the latter has been modified to match the toroidal curvature of the WEST plasmas. These are fed by 16 klystrons, each capable of providing 600 kW/CW on matched load, leading to a total generator power of 10 MW/CW. Eight of the klystrons, feeding the FAM launcher, have been tested on high power operation in Tore Supra [20]. Injection of LH power in the 5.0–6.0 MW range has been achieved in Tore Supra plasmas [21, 22].

The coupling of the RF waves to H-mode plasmas is one of the crucial points for WEST operation. To ease the LH wave coupling, local gas injection valves are installed at outer mid-plane locations, magnetically connected to the launchers [23]. This method may be particularly important for the FAM launcher, which needs a density of typically $\sim(3\text{--}5) \times 10^{17} \text{ m}^{-3}$ at the launcher mouth for optimum coupling. The ITER-relevant PAM launcher, on the other hand, has its optimum operating range close to the cut-off density ($1.7 \times 10^{17} \text{ m}^{-3}$ at $f = 3.7 \text{ GHz}$) and is therefore more suitable for operating in conditions with large plasma–launcher distance or with steep edge density gradients [24].

For the LH waves, the accessibility criterion implies that only waves with a launched parallel refractive index (N_{\parallel}) larger than a critical value can penetrate beyond a certain density. The choice of the launched parallel refractive index N_{\parallel} is a trade-off between the Stix–Golant accessibility condition and the current drive efficiency. The largest N_{\parallel} that allows the LH wave to penetrate in the core of the plasma and which can be excited by the PAM or the FAM launcher is 2.0. A LH wave with a given launched N_{\parallel} will couple to the plasma at the

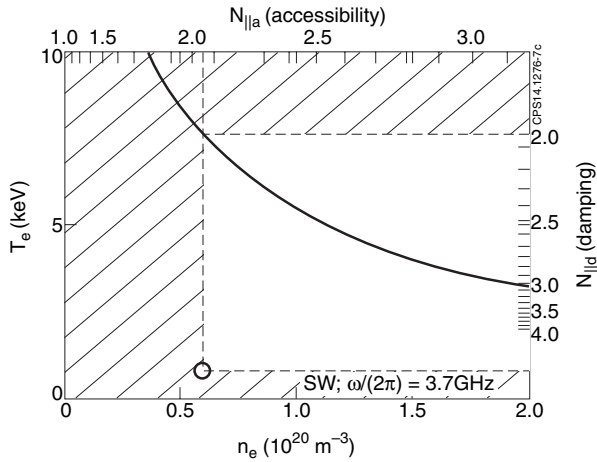


Figure 7. LHCD accessibility diagram at 3.7 GHz.

edge and propagate beyond the pedestal if the pedestal density is lower than the accessibility densities and if the pedestal temperature is lower than the temperature at which the linear Landau damping of the LH wave becomes strong [25]. These two conditions may be summarized in the diagram shown in figure 7. On the horizontal (respectively vertical) axis, the pedestal density (respectively temperature) is indicated. The corresponding $N_{\parallel a}$, for accessibility, and $N_{\parallel d}$, for Landau damping, are reported on their respective opposite sides. The full curve represents the condition $N_{\parallel a} = N_{\parallel d}$. The non-shaded area gives the range for which a given N_{\parallel} can propagate beyond the pedestal, without a strong Landau absorption or without being limited in radial penetration by the accessibility condition. For $N_{\parallel} = 2.0$, the pedestal density is limited to $6.5 \times 10^{19} \text{ m}^{-3}$ for the LH waves to propagate in the core of the plasma without prior multiple reflections between the caustic and the cut-off at the plasma edge, as shown in figure 7. The accessibility domain in figure 7 illustrates that the limit in temperature (around 8 keV) is well above the expected pedestal temperature, whereas a density limit of $6.5 \times 10^{19} \text{ m}^{-3}$ is in the expected range for the pedestal density as discussed later.

Additional sources of N_{\parallel} shifts are known to take place as the wave propagates in the plasma, as a consequence of toroidal refraction and other effects [25, 26]. Among the latter, the interplay of the wave in the SOL can also introduce a significant N_{\parallel} spectrum broadening at the separatrix [27, 28]. Modelling of injected $N_{\parallel 0} = 2.0$ cases has been carried out with the C3PO/LUKE codes [25, 26] for different pedestal densities, n_{ped} , as illustrated in figure 8 for $n_{\text{ped}} = 3 \times 10^{19}$ and $5 \times 10^{19} \text{ m}^{-3}$. The peak of the LH absorption occurs around mid-radius for both cases. In the low density range, the wave penetrates inside the plasma core, while, at high densities, it undergoes several reflections prior to its absorption. After multiple cut-off reflections, a strong $N_{\parallel 0}$ upshift takes place when the wave propagates in the vicinity of the X-point, which leads to a well off-axis LH wave deposition.

Thanks to fast electron bremsstrahlung tomography and extensive comparisons with existing ray-tracing and Fokker-Planck codes, WEST will bring new insights in LHCD physics at high pedestal density, together with Alcator C-Mod [29], EAST [30] and FTU [17]. On the technological side, high power operation of the PAM launcher during ELMs will allow

demonstrating that the PAM is a viable solution for LHCD in ITER [31].

3.2. Ion cyclotron resonance heating

WEST will be equipped with three new ICRH antennas, designed to provide resilience to ELMs as well as capacity for steady-state operation. Their design is an upgrade of the ITER-like ICRH prototype, tested in Tore Supra in 2007 [32, 33]. Their ELM resilience relies on vacuum conjugate T-junction. Due to the generator specifications, the maximum power available depends on the pulse duration: 3 MW/antenna during 30 s, 2 MW/antenna during 60 s and 1 MW/antenna in steady state.

The coupling of ICRH in H-mode plasmas is crucial and has longed been studied on Tore Supra plasmas [34]. Several gas injection points near the antennas are prepared, as well as reflectometry density measurement in front of the antennas in order to study the local SOL profiles. Comparing the observations with SOL 2D transport codes solving fluid equations such as SolEdge2D-EIRENE [35] will allow for detailed ICRH coupling studies.

It is planned to use ICRH mostly in the H minority scheme, i.e. damping by minority hydrogen ions in deuterium or helium at the fundamental cyclotron resonance. The nominal operating frequency is adjusted in order for the wave energy to be deposited in the central region to prevent W accumulation [36, 37]. However, due to the finite magnetic ripple level expected in WEST, the fast ions produced by ICRH can be deconfined [38]. As an illustration, figure 9 shows the good confinement region size which is affected by the value of the plasma current. In order to reduce the resulting fast ion losses, it is therefore desirable to retain the capability to locate the fundamental absorption layer in the good confinement region, by shifting it towards the high field side. To cover both the magnetic axis and access the good confinement zone even at low I_p , two frequency bands at the generator have been selected, as shown on figure 9, namely: 53 ± 2 and 56 ± 2 MHz.

The full wave solver EVE with the Fokker-Planck module AQL are used to model the ICRH deposition profiles [39]. Figure 10 illustrates an EVE/AQL simulation for 6 MW of ICRH at 55.5 MHz and $n_H/n_e = 6\%$. The power is deposited within $\rho = 0.4$, essentially on minority hydrogen ions (~ 5 MW). It is then redistributed through collisional relaxation of these fast ions between electrons (~ 2.5 MW) and bulk ions (~ 1.2 MW). As is often the case in the hydrogen minority scheme, the majority of the coupled power eventually heats electrons [40]. Some flexibility in terms of electron/ion heating can be obtained by varying the amount of ICRH power. When the coupled power is increased from 3 to 9 MW at $n_H/n_e = 6\%$, the mean energy of the fast ions increases [41] favouring collisional power transfers to the electrons [40]. This leads to an increase of the fraction coupled to the electrons from 45% to 70%, as illustrated by figure 11. Another possibility is to vary the minority hydrogen concentration, as shown in figure 12. When n_H/n_e is varied between 3% and 18% for 6 MW of coupled power, it is possible to transit from dominant electron heating to dominant ion heating. It should be noted, however, that operating at large minority concentrations can be difficult as the per-pass damping rate decreases as n_H/n_e increases.

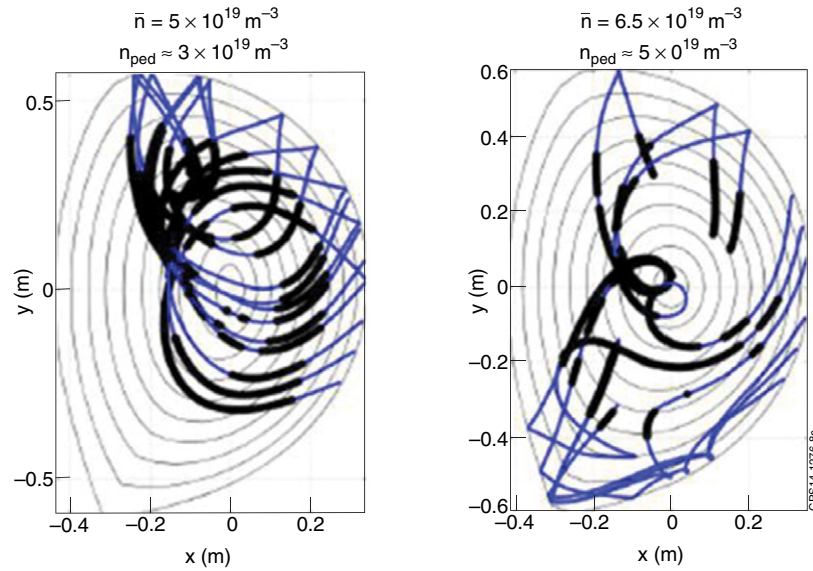


Figure 8. C3PO-LUKE LH modelling for two WEST scenarios.

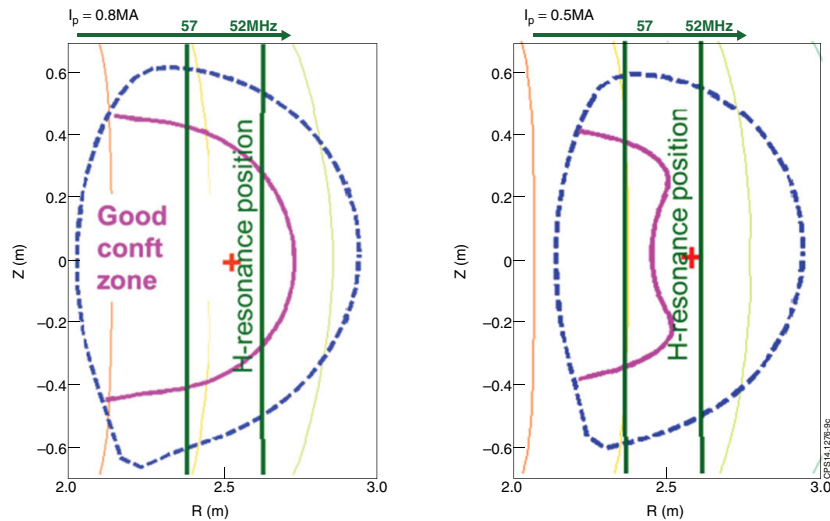


Figure 9. Poloidal views of WEST equilibria at 0.8 and 0.5 MA in steady state computed by CEDRES++ see figure 2. The unshifted H resonance positions are indicated in green for two ICRH frequencies: 52 and 57 MHz. In magenta are shown the limits of the good confinement region.

The optimization of ICRF scenarios constitutes an important research axis of WEST. Since the three new ELM resilient ICRH antennas can be operated in steady-state conditions, critical ITER topics such as continuous wave antenna operations, fast ion losses, central heating, the ratio of power to ions and electrons and impurity production from RF sheaths will be studied. The experimental results will be compared to ICRH codes such as SSWICH [42], EVE coupled with fast ion modules such as AQL [39] and SPOT [43].

4. Fuelling and pumping capabilities

Three fuelling systems are available in WEST: 19 gas puff injection lines connected to 11 calibrated reservoirs; three supersonic molecular beam injectors and four pellet injection points. Their capacities are of $11 \times 4 \text{ Pa m}^3 \text{ s}^{-1}$ for gas puff; of $3 \times 20 \text{ Pa m}^3 \text{ s}^{-1}$ for SMBI and of $7\text{--}11 \text{ Pa m}^3 \text{ s}^{-1}$ for the

pellets. In addition, a massive gas injection system (MGI) is available to mitigate the impact of disruptions and runaways. The system is designed to inject gas mixes (up to 5 bar l), with a delay of 5–10 ms to extinguish the plasma. Disruption mitigation experiments have been carried out previously with this system on Tore Supra to study various injection scenarios and to investigate gas jet penetration and mixing, showing in particular that runaway mitigation is more efficient using light gases [44]. Additional experiments on runaway mitigation have been performed using a high pressure cartridge [45]. This later system could be reinstalled in the WEST configuration if required.

During the discharges, active pumping is provided by 10 turbo-molecular pumps located at the bottom of pumping ducts under the baffle. The pumping baffle has been optimized to channel the neutrals towards the pumping systems, using the SolEdge2D–EIRENE code package [35]. SolEdge2D is a 2D

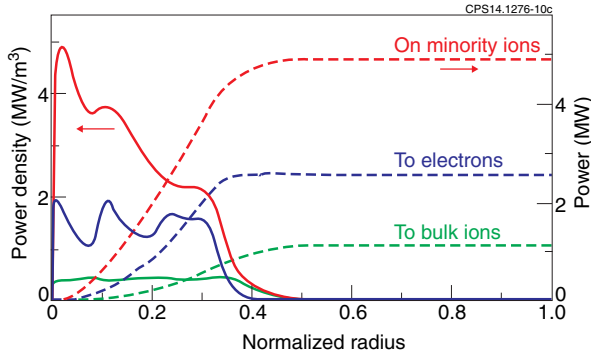


Figure 10. EVE/AQL modelling of a WEST scenario for 6 MW of ICRH at 55.5 MHz and $n_H/n_e = 6\%$. Power density absorbed by species (left y-axis, solid lines), total power (right y-axis, dashed lines).

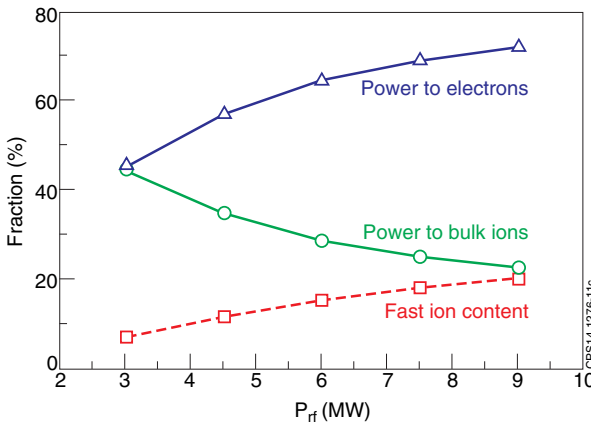


Figure 11. Power split between electrons and bulk ions (solid lines) when the coupled RF power is varied between 3 and 9 MW, at 6% minority concentration. Also shown is the fast ion content (dashed line).

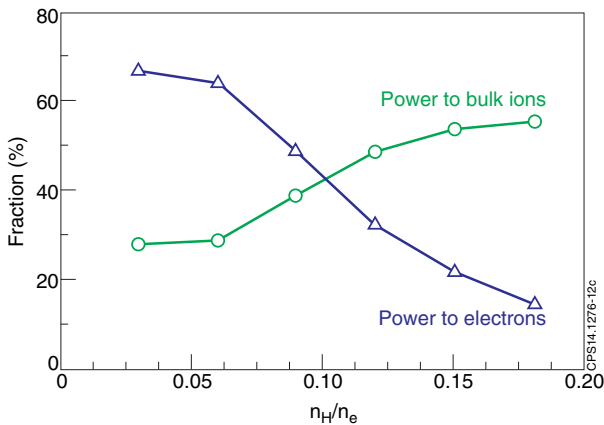


Figure 12. Influence of the hydrogen minority concentration on the power split between electrons and bulk ions.

transport code solving fluid equations for the plasma density, parallel momentum and temperatures for the main ions in a realistic geometry [35]. Sources related to neutral particles are calculated by the EIRENE kinetic transport code [46]. The SolEdge2D–EIRENE code package is run by puffing in D_2 molecules and imposing a given energy flux on the core–edge

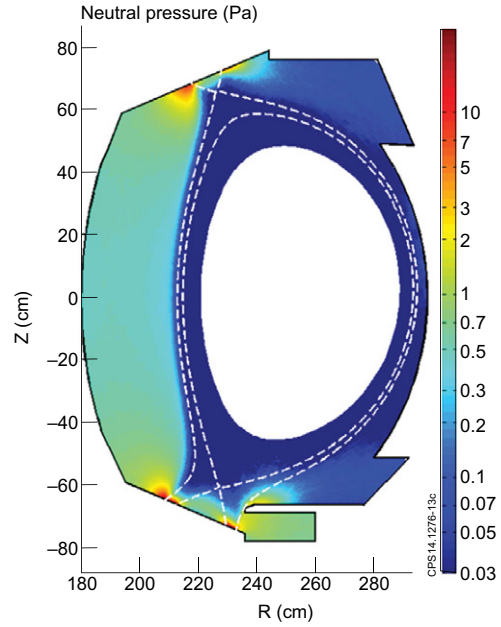


Figure 13. Neutral pressure in a poloidal cross section of WEST modelled by SolEdge2D–EIRENE [35].

interface. Simulations results indicate that the pressure under the baffle, with n_{sep} between 2 and $4 \times 10^{19} m^{-3}$, is expected to be in the range of 0.5–1 Pa, as illustrated in figure 13. This leads to a pumping rate of the order of $5 \times 10^{21} D s^{-1}$ or around $10 Pa m^3 s^{-1}$ which is consistent with the installed fuelling capabilities.

The WEST particle exhaust system provides a moderate pumping efficiency, as will be the case for ITER. The impact of low pumping capability on plasma operation (H-mode access, confinement quality, W sources) and fuel retention will be explored. The system could be upgraded to cryopumps depending on the results of the first phase of WEST operation.

5. L–H power threshold, pedestal and ELMs

The L–H power threshold has been estimated using different scaling laws. The ITPA 2008 scaling has been computed [47] as well as the ITPA 2004 one [48] where the impact of the effective charge Z_{eff} is included. The later has been recently shown to reduce the spread of JET-ILW and JET-C data points compared to the ITPA 2008 scaling law without Z_{eff} [49]. Moreover, since WEST has an aspect ratio, A , between 5 and 6, larger than most tokamaks, an additional aspect ratio dependence is discussed. The aspect ratio impact was reported by comparing spherical tokamaks with standard $A \sim 3$ tokamaks [48]. A higher P_{th} at lower A in [48] was found to be in qualitative agreements a scaling law based on ideas from [50].

Therefore, for WEST, the predictions from three scaling laws are illustrated in figure 14: ITPA 2008 [47], ITPA2004 [48] assuming $Z_{eff} = 1.2$ and ITPA 2004 with $Z_{eff} = 1.2$ and an additional aspect ratio impact such that $P_{th} \propto \frac{1}{\sqrt{A}}$ from [50]. Figure 14 shows the available additional power in WEST is larger than the most pessimistic of these scaling laws.

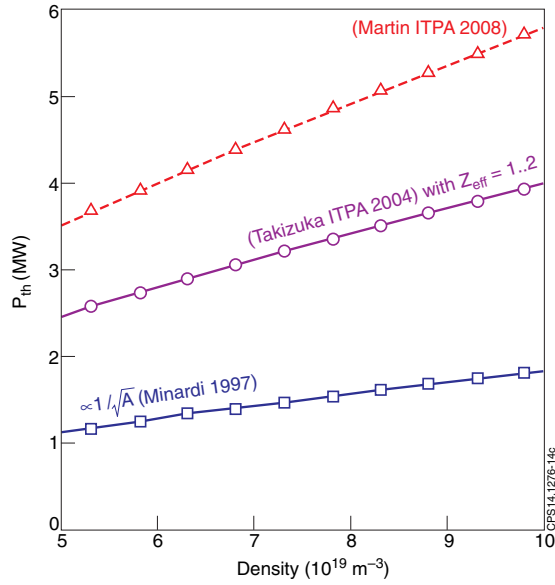


Figure 14. L–H power threshold expectation for WEST with respect to the core line average density. In red, triangles: ITPA 2008 [47]; in purple circles: ITPA2004 [48] assuming $Z_{\text{eff}} = 1.2$; in blue squares: ITPA 2004 with $Z_{\text{eff}} = 1.2$ and an additional aspect ratio impact such that $P_{\text{th}} \propto \frac{1}{\sqrt{A}}$ from [50].

On the experimental side, the WEST compact divertor geometry has been tested in the W environment of ASDEX Upgrade and a power threshold of 2 MW was reported [51].

Nonetheless, uncertainties remain, in particular in WEST the magnetic field ripple reaches around 2% at the outboard mid-plane boundary and it could affect the L–H power threshold through the modified ambipolar radial electric field. Note however that in JET a ripple up to 1.1% did not affect the threshold [52] and in JT-60U, before the installation of ferromagnetic inserts, the power threshold was even reduced with larger magnetic ripple [53]. In DIII-D, local magnetic ripple of 3% from test blanket module mock-up coils did not change P_{th} [54].

The ideal MHD stability limit in the WEST scenarios studied has been calculated using the linear MHD code MISHKA [13]. The pedestal width is assumed to be around 5% of the minor radius such that $\Delta_{\text{ped}} = 2.3$ cm. A pedestal pressure limited by the ballooning limit of 14.5 kPa was found for $I_p = 0.8$ MA, see figure 15. This limit scales with I_p^2 , hence, at 0.5 MA, 6 kPa are expected.

The impact of WEST large aspect ratio, ranging from 5 to 6, on the pedestal height and width remains to be studied. For the time being, the scenarios are prepared with a pedestal energy derived from the multi-machines ITPA scaling law given in [55] and leads to consistent pedestal pressures within 65% to 90% of the ideal MHD limit with $\Delta_{\text{ped}} = 2.3$ cm.

Using the ITPA 2007 pedestal energy scaling law [55], it is found that the pedestal energy, W_{ped} , is in the range of 20–25% of the total thermal energy, W_{th} , in WEST modelled scenarios presented in section 8. For the high power scenario illustrated by table 1, a maximum W_{th} of 0.9 MJ is expected with a H_{98} factor of 1. This means that up to W_{ped} of 200 kJ is anticipated. The ratio $W_{\text{ELM}}/W_{\text{ped}}$, where W_{ELM} is the energy expelled per ELM, varies with collisionality for baseline discharges [57]

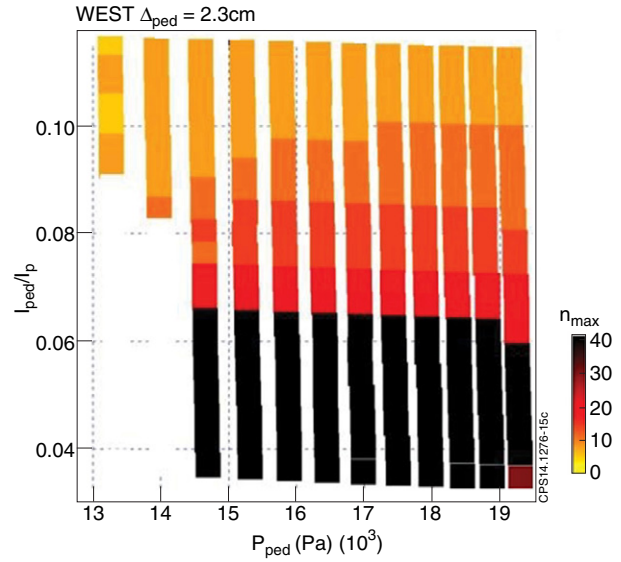


Figure 15. Ideal MHD limit computed by MISHKA [56] for $I_p = 0.8$ MA. The low wave number modes are the peeling modes and the higher wave number modes are the ballooning modes.

but for hybrid scenarios no clear correlation can be established [58]. $W_{\text{ELM}}/W_{\text{ped}}$ can be as low as a few % and as high as 20% in the case of low density type I ELMs. Therefore, ELMs of up to 40 kJ are anticipated. The size of the wetted area will depend on the X-point height and on the broadening of the wetted area. For a high X-point height around 10 cm, without broadening, and without divertor tile shaping, a wetted area in the range of 0.3 m^2 is expected. Accordingly, in this case, an ELM load of more than 100 kJ m^{-2} could be reached. Using [59], the associated ELM frequency, f_{ELM} , can be estimated as follows: $f_{\text{ELM}} = 0.2 \times P_{\text{SOL}} (\text{MW}) \times 10^3 / W_{\text{ELM}} (\text{kJ})$, leading to $f_{\text{ELM}} = 50$ Hz for the high power scenarios and $W_{\text{ELM}} = 40$ kJ.

On a scenario with 10 MW m^{-2} onto the divertor, the tile surface temperature reaches 1100°C . In the case of type I ELMs with $W_{\text{ELM}} = 40$ kJ at 50 Hz, temperature excursions of 300° on the surface of the actively cooled W monoblocks are modelled by finite element method thermal simulations [8] as illustrated by figure 16. Hence, with such ELMs, cycling around the W recrystallization temperature, i.e. above 1200°C , would allow studying the actively cooled W divertor response. Experiments in WEST accumulating 100 000 transients or more would be benchmarked against laboratory experiments to assess the role of possible synergistic effects encountered in a tokamak environment. As an alternative to the utilization of large ELMs, the use of an *in situ* laser tool to study the impact of combined transient/steady-state heat loads is considered.

ELMs study is a strong axis of research in WEST integrating physics, operational and technological aspects. The impact of resistivity and aspect ratio on ELMs will be studied and compared to codes such as JOREK [60] and MISHKA [56]. The heat loads on the divertor will be monitored taking advantage of the 100% coverage of the lower divertor by infrared thermography and thanks to probe measurements and thermocouples. Fast and high resolution infrared cameras are foreseen to explore the ELM wetted area and its modification with ELM size. Finally, the impact of more than 100 000 transients on ITER-like actively cooled W

Table 1. Summary of some key parameters characterizing 3 scenarios for WEST suited with the code METIS.

Scenario	High power	Standard	High fluence
I_p (MA)	0.8	0.6	0.6
n_e (10^{19} m^{-3})	8.0	7.0	7.0
f_{GW} (%)	70	70	70
P_{heat} (MW)	15	12	10
LHCD (MW)	6	6	7
ICRH (MW)	9	6	3
P_{rad} (MW)	5.0	3.0	3.0
β_N	2.7	2.2	1.7
T_{ped} (keV)	0.7	0.4	0.4
n_{ped} (10^{19} m^{-3})	5.0	5.0	4.5
W_{th} (MJ)	0.9	0.6	0.5
Bootstrap fraction (%)	30	35	35
LHCD fraction (%)	30	50	60
Pulse length (s) min(14 Wb or IC time limit)	30	60	1000
Expected heat load (MW m^{-2}), 2/3 versus 1/3 asym.	10 to 20 depending on X-point height and λ_q		
Operation time to reach one ITER pulse fluence	–6 months	–2 months	Few days

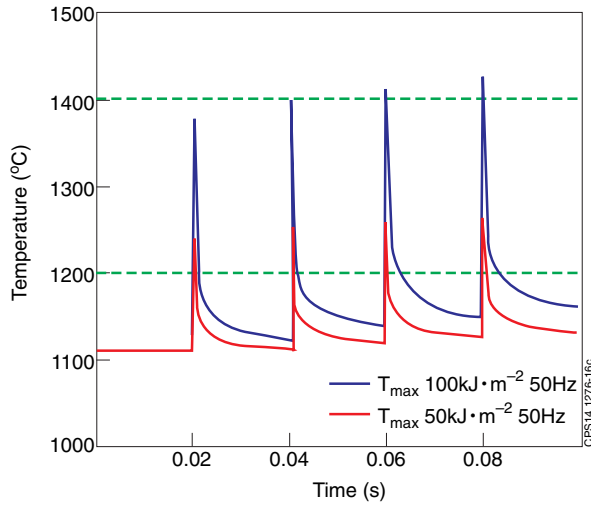


Figure 16. Estimate of the temperature increase of the W monoblocks linked to ELMS, for a steady-state heat load of 10 MW m^{-2} , and large type I ELMS of 50 and 100 kJ m^{-2} , red and blue curve respectively, 50 Hz frequency with a rising time scale of $400 \mu\text{s}$. The W recrystallization temperature range is bordered by green dashed lines.

divertor targets will be studied *in situ* using the articulated inspection arm and post-mortem analysis.

6. Expected density profiles

The density profile prediction for WEST is based on three estimates: the density at the separatrix, the pedestal density and the core density peaking factor.

As expected from the 2 points model [61], the plasma temperature downstream on the divertor target is constrained by the density at the separatrix. The upper bound considered in the following is of the order of 50 eV , a temperature above which W sputtering by deuterium sharply increases [62]. Figure 17 shows the target temperature from the 2 points model with hydrogen recycling included. The electron cooling of 25 eV per ionization event is taken, and the 2 points model parameters are such that $f_{\text{mom}} = 0.8$, $f_{\text{cond}} = 1$ [61]. Different fractions of the power loss in the SOL ($P_{\text{loss}}^{\text{SOL}}$) with

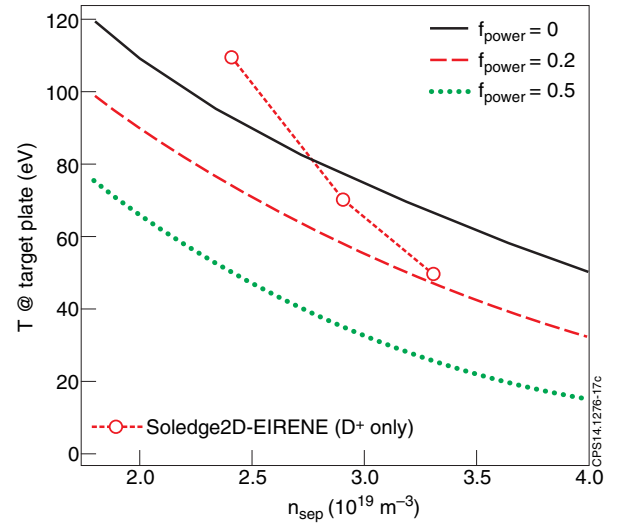


Figure 17. Plasma temperature in front of the target plates as a function of separatrix (upstream) density from a two points model, for $P_{\text{SOL}} = 6 \text{ MW}$ and $\lambda_q = 5 \text{ mm}$ and various levels of radiated power in the SOL. Open circles are pure deuterium SolEdge2D–EIRENE calculations for the same parameters.

respect to P_{SOL} are explored such that $f_{\text{power}} = P_{\text{loss}}^{\text{SOL}}/P_{\text{SOL}}$ is varied from 0% to 50% . Here a fairly high power case is considered with $P_{\text{SOL}} = 6 \text{ MW}$, $\lambda_q = 5 \text{ mm}$, i.e. a combination of parameters which should allow reaching 10 MW m^{-2} on the divertor plates, and relevant for H-mode operation (see sections 2 and 5). Should λ_q be lower, P_{SOL} should be lower too in order to be compatible with safe PFC operation. This simple model shows that high power operation requires separatrix densities of the order of $3 \times 10^{19} \text{ m}^{-3}$. These estimations for the required separatrix density are in fair agreement with SolEdge2D–EIRENE modelling [35] (pure deuterium cases) see open circles in figure 17 from [63]. In SolEdge2D–EIRENE a particle diffusion coefficient D has been chosen such that $D = 0.3 \text{ m}^2 \text{ s}^{-1}$, a convection velocity such that $v = 0.1 \text{ m s}^{-1}$ and the assumed diffusive heat transport such that $\chi_e = \chi_i = 1 \text{ m}^2 \text{ s}^{-1}$. Note that these transport coefficients are compatible with an analysis of the heat deposition profiles leading to $\lambda_q \approx 5 \text{ mm}$.

In metallic machines, in H-mode, the operation at low densities is more limited than in C wall machines. Indeed, JET-ILW [64] and ASDEX Upgrade with the full W coverage [15, 65] both operate in a $n_{\text{ped}}/n_{\text{gw}}$ range, from 40% to 80%. In WEST, for $I_p = 0.6\text{--}0.8$ MA, the Greenwald density, n_{gw} , ranges from 10 to $12 \times 10^{19} \text{ m}^{-3}$. Therefore n_{ped} between 4 to $9 \times 10^{19} \text{ m}^{-3}$ is expected.

On the other hand, a multi-machine database shows that $n_{\text{ped}}/n_{\text{sep}}$ correlates with $n_{\text{sep}}/n_{\text{gw}}$ [66]. As discussed above, n_{sep} of the order of $(2\text{--}3) \times 10^{19} \text{ m}^{-3}$ is projected, i.e. $0.15 \leq n_{\text{sep}}/n_{\text{gw}} \leq 0.3$. Therefore based on [66], n_{ped} between 3 and $9 \times 10^{19} \text{ m}^{-3}$ are anticipated. This range is coherent with the previously expected constraint on $n_{\text{ped}}/n_{\text{gw}}$.

The density peaking factor has been extensively studied in H-modes in JET and ASDEX Upgrade [67]. Multiple regression analyses show that in the combined database collisionality is the most relevant parameter. Based on these works, a core density peaking with $\frac{n_0}{\langle n \rangle} - 1 = 0.28\text{--}0.17 \ln \nu_{\text{eff}}$ from [68] is used for WEST scenarios extrapolation, where ν_{eff} is the normalized collisionality, n_0 the central electron density and $\langle n \rangle$ the volume averaged electron density. It is to note that WEST has an aspect ratio significantly larger than JET and ASDEX Upgrade, 5 to 6 in WEST to be compared to 3 in JET and ASDEX Upgrade. A larger aspect ratio is expected to modify the core turbulent transport due to a reduced trapped particle fraction, in particular trapped electron modes should be less unstable. The high aspect ratio in WEST will expand the existing databases beyond possible future DEMO values of about $A = 4$, allowing firmer projections from the large existing $A = 3$ database. This means that ideally the core particle transport in the large aspect ratio WEST should be modelled using first principle transport codes such as TGLF [69] or QuaLiKiz [70] in CRONOS [71]. Such studies are planned. For the time being, the modelled density profile peaking is based on [68].

Since WEST will operate without NBI, hence without central particle fuelling, and at low loop voltage, hence reduced neoclassical Ware pinch, core particle transport at high aspect ratio will be analysed as done in the past [72]. The density profiles will be measured precisely thanks to a full coverage by reflectometry measurements together with 10 interferometry chords. The peaking factor will be compared to first principle non-linear and quasilinear gyrokinetic codes [70, 73].

7. W sources and contamination

Experience from ASDEX Upgrade and JET shows that tungsten sources as measured by spectroscopy are usually dominated by W sputtering caused by light impurities [15]. This is due to (1) the fact that even in the inter-ELM regime sputtering by light impurities is usually not extinguished, and (2) the contribution of ELMs [62]. In ASDEX Upgrade, the main chamber tungsten source is dominant for the core plasma W content, due to the efficient divertor retention for sputtered W. So, it should be stressed that one of the main source of uncertainties in foreseeing W sources in WEST is the fact that the concentration of light impurities (O, C, B) cannot be predicted accurately. Preliminary calculations with SOLPS4.0 and DIVIMP including C as a representative impurity have shown tolerable contamination levels, that is, comparable to

those observed in ASDEX Upgrade, for conditions where peak heat fluxes are of the order of 10 MW m^{-2} [74]. These simulations have been made assuming that the power flowing through the separatrix is such that $P_{\text{SOL}} = 4\text{--}8$ MW. A specific feature of a W machine compared to a low- Z machine is the existence of potentially strong core–edge coupling, due to the fact that W radiates in the core. As a result, an increase of W sources and thus contamination would reduce P_{SOL} at a given injected heating power, hence lower the temperatures in front of the target plates and in turn act as a feedback on W sources [75]. Roughly speaking, the temperature in the divertor would then settle around the effective sputtering threshold value, for the mix of low- Z impurities present in the plasma. This situation pertains to low density cases, for which W screening is inefficient. At higher densities, one would expect lower W contamination, hence lower radiation losses in the core and thus reduced core–edge coupling. Addressing the full picture is very challenging, because core transport physics (accumulation, saw teeth) and pedestal physics (transport through the pedestal, ELMs flushing) have to be taken into account. However, simplified tools such as Corediv, which simulates both core and edge plasmas have proven to be valuable to analyse ASDEX Upgrade and JET discharges [76]. Coupled core–edge modelling for WEST has been performed with Corediv first in pure deuterium [77]. Then, to mimic a light impurity content, boron is included as a typical light impurity [63]. In these simulations, a concentration of boron of 1% typically reduces the power flowing to the target plates by 50% compared to a pure deuterium case, essentially due to W radiation in the core (edge radiation by boron is then comparable to deuterium radiation) for coupled power above 8 MW and a volume averaged density of $6 \times 10^{19} \text{ m}^{-3}$. As an illustration, figure 18 shows the radiation fraction in the core and in the SOL for a heating power of 14 MW, as a function of boron concentration in %. In these simulations, the edge radiation is fairly low because boron is not an efficient radiator. Also, reaching $P_{\text{SOL}} = 6$ MW as assumed e.g. for figure 17 would then require about 12 MW of auxiliary power. Note that estimates for the peak power flux density in section 2 assumed 40% of coupled power radiated, and are thus consistent with these results.

However, even if W divertor sources are dominant in terms of gross sputtered fluxes, the contamination of the main plasma seems to be often controlled by main chamber sources [62, 78], which were not included in either the SOLPS/DIVIMP or Corediv simulations mentioned earlier. It should be emphasized that in WEST most of the first wall elements are farther from the plasma than in ASDEX Upgrade, with the exception of a few objects such as the pumping baffle and the antenna guard limiters. Also, unlike most other machines, all the antennas on WEST are moveable radially in the chamber [34]. While a low radial gap between the radiating straps and a characteristic density layer is beneficial for the ICRH power coupling, a minimal antenna–separatrix clearance was found necessary on Tore Supra to maintain safe steady-state surface temperatures on the antenna structures [34]. Similar operational trade-off will probably have to be found in WEST to limit the impurity accumulation in the main plasma over long pulses. In this empirical optimization, localized gas injection in the main chamber might also influence the impurity

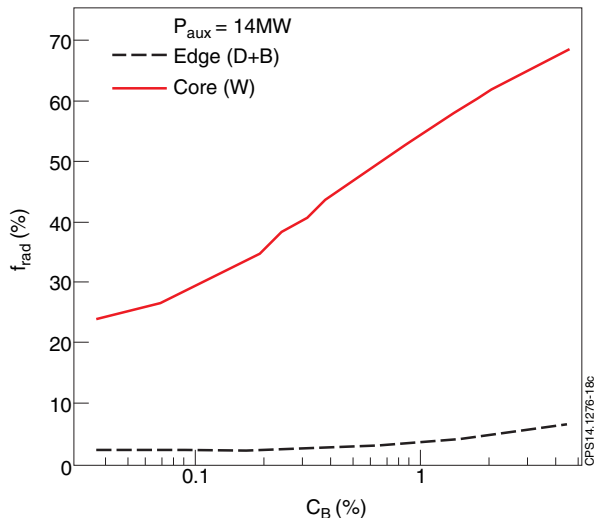


Figure 18. Fraction of the heating power radiated in the core (solid red) and in the edge (dashed black), as a function of boron concentration in % obtained by Corediv for $P_{\text{aux}} = 14$ MW. Core radiation is almost exclusively from W while edge radiation is essentially from D and B.

production near the antennas, as suggested experimentally on ASDEX Upgrade [14] and JET [37].

Calculating main chamber sources is a challenge for modelling since most of the current versions of transport codes cannot simulate the plasma up to the first wall. This issue is currently being addressed with the SolEdge2D–EIRENE code [79], and first calculations of W sources have been presented in [80]. But these simulations will have to be complemented by additional modelling to address a possible influence of turbulent fluctuations in the far SOL (filaments) [81], penetration of neutrals [82] and transport of impurities in such fluctuating plasmas [83]. Last but not least, prompt redeposition has to be taken into account [84]. The latter is shown to play an important role in the balance between divertor and main chamber sources, as illustrated on figure 19. In the simulations presented in [80], the pumping baffle is found to be a substantial source of W (between 15% to 40% of the total net W influx, with prompt redeposition taken into account, in the absence of ICRH). DIVIMP modelling has been initiated to provide an estimate for the W contamination resulting from these sources.

Finally, it must be emphasized that calculations presented on figure 19 do not take the effect of ICRH operation into account (hence the sources on the antenna limiters are underestimated [14, 16]). It should also be mentioned that these 2D simulations do not take the limited toroidal extent of the antenna limiters into account, so that the sources reported on figure 19 (with ICRH switched off) are actually overestimated. In addition, the antennas are movable, so that their position in the simulations is only representative of a typical situation. One expects enhanced potentials in region magnetically connected with the antennas [85] and a maximum of the potential is observed in region connected with the antenna side limiters [86–89]. Nonetheless, it is still difficult to extrapolate because enhanced potentials are also observed in unconnected regions on Alcator C-Mod [85], in some cases similar enhanced potentials are measured with

an unexpected smaller impurity production [87]. ICRH-induced convective cells are also supposed to enhance the perpendicular penetration of the impurities [89]. Therefore, predicting the W sources during ICRH operation from first principle is not possible at this time. The sources will depend on the type of antenna, on its operation mode, as well as light impurity concentrations and conditions in front of the antenna (fluxes, ionization degree). Nevertheless, experience gained during Tore Supra operation in L-mode can be used to estimate particle fluxes and typical ion energies on the antenna protections [90, 91]. Both probe data mapped onto the antenna protections and analysis of IR data lead to particles fluxes of up to a few $10^{22} \text{ D}^+ \text{ m}^{-2} \text{ s}^{-1}$, and ions energies of the order of 200 eV. Using an ASDEX Upgrade relevant effective sputtering yield of $Y_{\text{eff}} \sim 10^{-4}$, one typically would get gross tungsten influxes in the range $\Gamma_{\text{W}} = 10^{18} \text{--} 10^{19} \text{ m}^{-2} \text{ s}^{-1}$ if the WEST antennas are operated in similar conditions as on Tore Supra, i.e. with a strap potential between 10 to 30 kV. The surface area of the antenna limiter, assuming that the three ICRH antennae are operating, is of the order of 0.1 m^2 . The total W influx can thus be estimated as $10^{17} \text{--} 10^{18} \text{ s}^{-1}$, noting that prompt redeposition is likely to be low (as observed on figure 19) because of the fairly low modelled temperatures in front of the antennas in absence of sheath rectification. These values are comparable to those obtained in SolEdge2D–EIRENE simulations for the net divertor sources (i.e. including prompt redeposition effects), while easier W penetration to the plasma core is expected from the antenna limiters than from the divertor. From this analysis, it can be concluded that W sources on antenna protections are indeed likely to play a substantial role in the W contamination, as is the case elsewhere [87]. Note that enhanced floating potentials during ICRH were measured by Langmuir probes located at the top of Tore Supra, several meters away toroidally from the powered antennas [88]. Therefore ICRH operation might also increase sources elsewhere in the machine, in particular on divertor baffle and target areas magnetically connected to the antennas.

In order to address these issues, the W sources will be closely monitored thanks to the comprehensive visible spectroscopy diagnostic which will be available on WEST, with 200 lines of sight aiming at both divertors, baffle, antenna limiters and inner bumpers. The compact divertor geometry allows good optical access to study the physics of, e.g. prompt W redeposition. The good diagnostic coverage of antenna protections will be an asset for HF sheaths code validation [92].

8. Integrated standard scenarios

The integrated modelling of WEST scenarios has been performed with the 0D version of CRONOS code called METIS [71]. METIS stands for Minute Embedded Tokamak Integrated Simulator. 300 time slices are modelled within one minute. The heat transport equations are simplified by separating the time and radial dimensions, which allows a fast solution to the heat transport problem based on scaling law prescriptions. The current diffusion is carried out in 1.5D with moment equilibrium, as in traditional integrated modelling solvers. The heat and particle source profiles are deduced from simple models. The global energy content comes from 0D scaling laws. The temperature profiles are stationary 1D

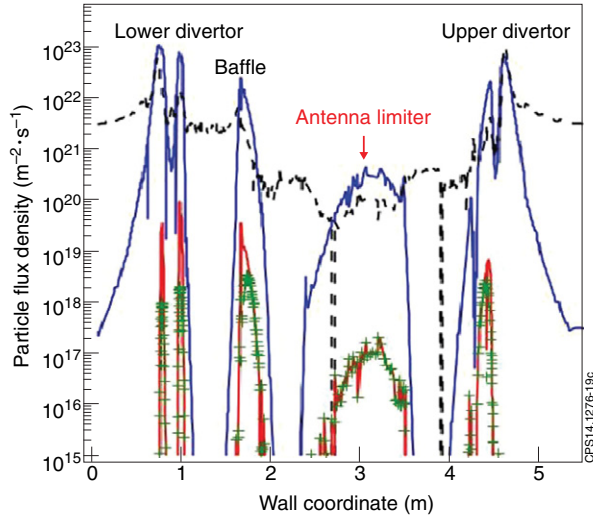


Figure 19. Particle flux densities as a function of the poloidal location, from the lower to the upper divertor via the low field side elements (baffle and antenna limiters). D^+ flux (solid blue), D flux (dashed black), W gross influx from ions (solid red) and net influx from ions (green crosses), i.e. accounting for prompt redeposition, but without sheath rectification.

solution scaled to reproduce W_{th} . All non-linearities are solved (dependence of sources on profiles etc). The inputs are: the additional power, I_p , the line average density, Z_{eff} , the LCFS geometry. The outputs are all standard 1D and 0D data from a transport code. METIS is included in the CRONOS suite of codes, as a first step scenario design to prepare full integrated modelling simulations.

Before using METIS to predict WEST scenarios, it has been used to model eleven JET-ILW and one ASDEX Upgrade pulses. With a choice of reasonable sets of input parameters, METIS outputs could simultaneously reproduce the energy content, the radiated power level as well as the density and temperature profiles, in particular the pedestal and LCFS values. One of the pulses used is shown on figure 20. It is a JET-ILW pulse with ICRH and NBI heating. The thermal energy content, W_{th} , is reproduced by adjusting the H factor [93]. H factors ranging from 0.7 to 1 have been found, for the case of figure 20(a), $H = 0.8$ has been required. The radiated power, P_{rad} , is reproduced using the revised W cooling rate [94], assuming flat W profiles and adjusting C_W at the LCFS. C_W from 1 to 7×10^{-4} has been found necessary to reproduce the core P_{rad} value, for the case of figure 20(a), $C_W = 7 \times 10^{-4}$ has been required. The separatrix density value is from the scaling proposed in [95] and agrees well with the measured values, as it can be seen for the example illustrated by figure 20(c). The pedestal width is fixed and chosen to be 5% of the minor radius. The pedestal density is then constrained by the line average density and the density peaking chosen, here [68]. In some cases, density peaking from [68] leads to underestimated n_{ped} as in can be seen for the case illustrated on figure 20(c). T_{ped} is deduced from W_{ped} based on [55] multiplied by the H factor. It is usually in good agreement with the measured values, as illustrated for one of the cases on figure 20(d).

Based on a fair agreement obtained on these 12 cases and using the information gathered through the previous reported studies (ICRH, LHCD, pedestal density value, W content,

etc), WEST pulses have been modelled. For ICRH a power absorption within $\rho = 0.4$ is modelled, based on EVE/AQL results of section 3, with a ratio of 50% of the power coupled to the bulk ions and 50% to the electrons (see figure 10). LH waves are absorbed at mid-radius (see figure 8) with a CD efficiency from 0.07 to $0.1 \times 10^{20} \text{ A W}^{-1} \text{ m}^{-2}$ consistent with C3PO/LUKE simulations reported in section 3. The density peaking from [68] is used, based on the relative success in reproducing JET profiles. A density at the separatrix from [95] coherent with SolEdge2D–EIRENE expectations presented in section 6 is assumed. A pedestal width of 5% is taken, which was found coherent with JET observations as illustrated by figure 20(c). A W concentration at the separatrix such that $n_W/n_e = 5 \times 10^{-4}$ is taken, in the range used to reproduce the radiated power of the 12 studied cases. Such a W concentration is in the right order of magnitude, in case of target temperatures around 50 eV and some light impurity content [62] as presented in section 7. A flat n_W profile is assumed for the moment. In the future simultaneous turbulent and neoclassical transport should be accounted for. The radiative power, P_{rad} , is determined using the revised W cooling rate from [94]. The H factor from [93] is taken to be 1 and sensitivity tests in the range 0.7 to 1.2 have been carried out. The pedestal energy based on the ITPA scaling [55] adjusted to the H factor is used. It was shown to be below the ideal MHD limit for $\Delta_{ped} = 2.3 \text{ cm}$ in section 5 and to reproduce well 12 cases as the one illustrated on figure 20(d).

All scenarios are for 3.7 T at 2.5 m. Accounting for the fact that ICRH power is limited by the generator to 9 MW/30 s, 6 MW/60 s or 3 MW/1000 s, three types of scenarios have been designed. The high power one with 9 MW of ICRH and 6 MW of LH lasting 30 s at 0.8 MA; so-called ‘standard’ cases with 6 MW of ICRH and 6 MW of LH lasting 60 s at 0.6 MA (and lasting less if operated at higher current, 25 s at 0.8 MA) and finally a high particle fluence scenario lasting 1000 s with 3 MW of ICRH and 7 MW of LH power. The three scenarios are summarized in table 1.

In particular, one can note that the Greenwald fraction is between 60% to 70%, which is coherent with the fraction at which metallic wall machines such as JET-ILW [64] and ASDEX Upgrade [65] routinely operate. The pedestal density is at most $5 \times 10^{19} \text{ m}^{-3}$ which should be compatible with LH wave accessibility discussed in section 3. The bootstrap fraction is around 30–35% and the fraction of LH driven current up to 60%. On figure 21, the profiles for the 3 scenarios are illustrated. The density profiles are peaked due to the scaling used [68], this should be revisited using CRONOS and realistic transport codes. The electron temperature reaches up to 6 keV in the core of the high power case. The q profiles do not go below 1 for the two scenarios at 0.6 MA. The q profile is even expected to be strongly reversed in the high fluence scenario due to the off-axis LHCD absorption. No ITB model has been included here.

Moreover advanced tokamak modes are expected to be accessible thanks to the LHCD long-pulse capability at high power and their investigation will be an important research axis of WEST. Note that a 30 s pulse is as long as 20 resistive times. These scenarios will allow developing real-time control expertise for long pulse scenarios, exploring some advanced regimes and their control. This programme will participate to JT60-SA operation preparation.

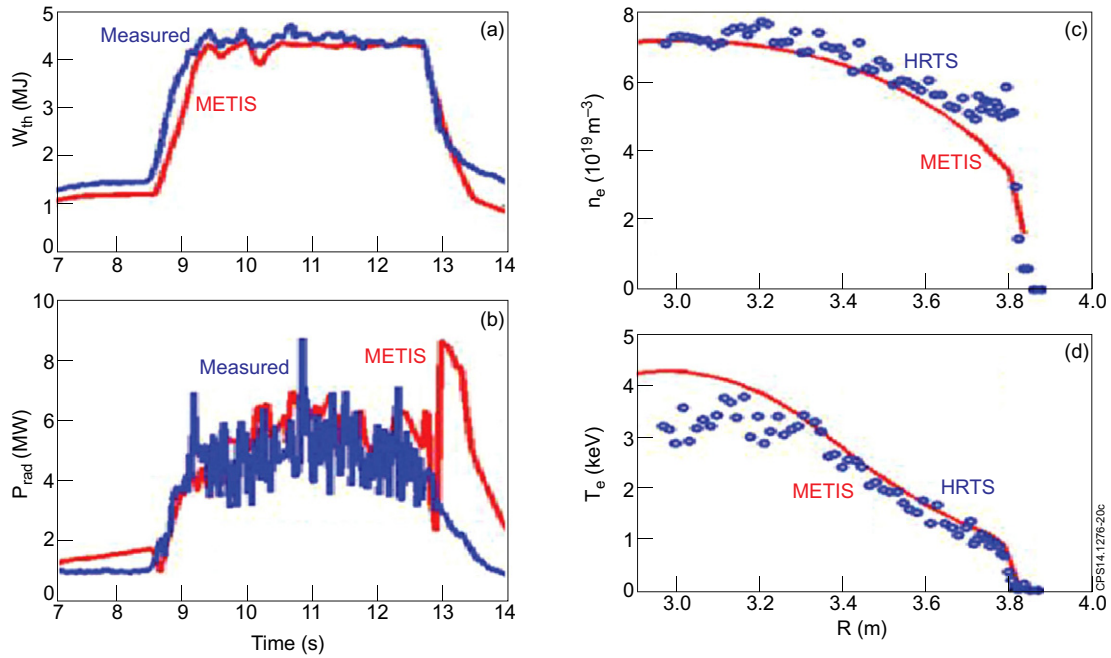


Figure 20. JET-ILW pulse 84746. (a) The thermal energy versus time. In blue the measured one and in red the simulated one with METIS. (b) P_{rad} versus time in s. (c) The electron density profile at 11 s measured by HRTS in blue and modelled by METIS in red. (d) The electron temperature profile at 11 s.

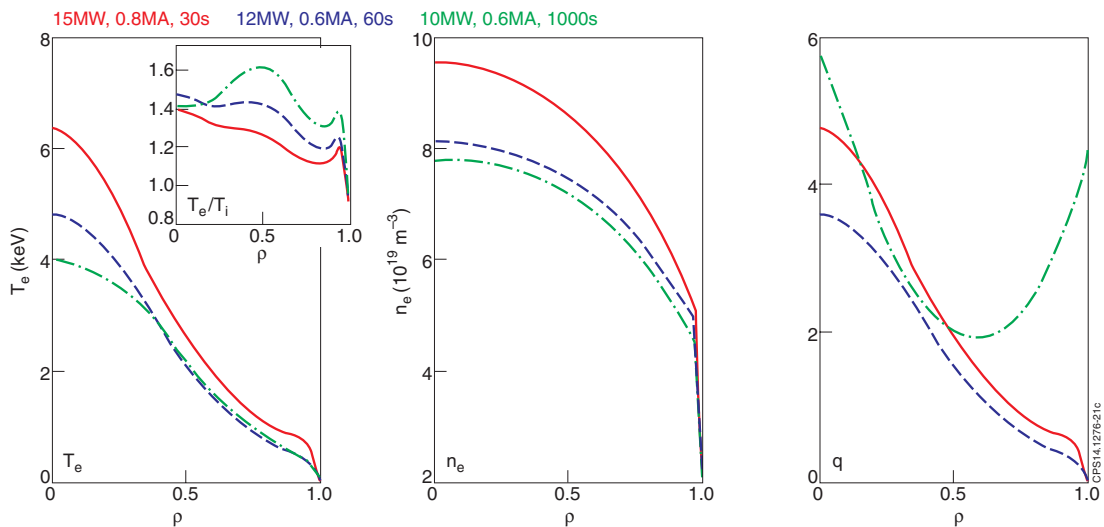


Figure 21. Temperature, density and q profiles of the 3 scenarios summarized in table 1.

9. Conclusions

Sustainment of ELMy H-mode up to 1000 s with 10–20 MW m^{-2} onto the divertor is achievable. WEST will thus allow operating an actively cooled tokamak equipped with an ITER-like divertor and studying simultaneously the related technology, operation and physics a phase ahead of ITER. The WEST scientific programme has been discussed extensively during the 1st WEST International in Aix-en-Provence, France, from June 30 to July 2, 2014 [WWS14]. It is organized around two main axes: ‘ITER grade PFC tests’ and ‘towards long pulse H-mode and steady-state operation’. WEST operation is to be started in 2016 [2].

The research activities on WEST will address a very large variety of topics such as: steady-state and transient heat loads on an ITER-like actively cooled tungsten divertor, infrared monitoring of the surface temperatures in a metallic environment, LHCD absorption at high density, ICRH coupling with ELMs, W source survey and understanding, density control over long time, large aspect ratio impact on core turbulent transport, W transport, L–H power threshold in large aspect ratio machine, advanced tokamak scenarios, etc. A helium campaign is also foreseen to address PFC and confinement ITER-relevant issues.

The WEST platform and its research plan are fully open to all ITER partners. It will contribute to train professionals

and newcomers on a long pulse superconducting tokamak integrating high heat flux tungsten PFCs and thus actively prepare ITER divertor operation

Acknowledgments

The authors wish to acknowledge the active and fruitful participation to the 1st WEST International Workshop of D. Campbell, F. Escourbiac, R. Pitts and J. Snipes from ITER Organization, P. Lorenzetto from F4E, K. Ezato from JADA, X. Litaudon from EUROfusion, D. Hillis from ORNL, C. Angioni, V. Bobkov and Th. Eich from IPP Garching, S. Brezinsek, J. Coenen, C. Linsmeier and T. Loewenhoff from FZJ, S. Kajita from Nagoya University, A. Tuccillo from ENEA and P. Chiappetta from Aix-Marseille University. This work has been carried out within the framework of the EUROfusion Consortium and has received funding from the European Union's Horizon 2020 research and innovation programme under grant agreement number 633053. The views and opinions expressed herein do not necessarily reflect those of the European Commission. The views and opinions expressed herein do not necessarily reflect those of the European Commission.

References

- [1] Pitts R.A. 2013 *J. Nucl. Mater.* **438** S48
- [2] Bucalossi J. et al 2014 *Fusion Eng. Des.* **89** 907–12
- [3] <http://west.cea.fr/Workshop2014/>
- [4] Missirlan M. et al 2014 *Fusion Eng. Des.* **89** 1048–53
- [5] Heumann H. and Blum J. 2014 *SIAM J. Sci. Comput.* submitted <https://hal.archives-ouvertes.fr/hal-00988045>
- [6] Eich T. et al 2011 *Phys. Rev. Lett.* **107** 215001
- [7] Firdaouss M. et al 2015 *Fusion Eng. Des.* in press <http://dx.doi.org/10.1016/j.fusengdes.2014.12.024>
- [8] Courtois X. et al 2013 *Fusion Sci. Technol.* **64** 727–34
- [9] Loewenhoff Th. 2012 Combined steady state and high cycle transient heat load simulation with the electron beam facility JUDITH 2 (RWTH Aachen, 2012) *PhD Thesis* <http://darwin.bth.rwth-aachen.de/opus3/volltexte/2012/4313/>
- [10] Wirtz M. et al 2013 *J. Nucl. Mater.* **443** 497–501
- [11] De Temmerman G. et al 2013 *Nucl. Fusion* **53** 023008
- [12] Bucalossi J. et al 2011 *J. Nucl. Mater.* **415** S832–5
- [13] Mayoral M.-L. et al 2014 *Nucl. Fusion* **54** 033002
- [14] Bobkov V. et al 2013 *Nucl. Fusion* **53** 093018
- [15] Neu R. et al 2011 *Plasma Phys. Control. Fusion* **53** 124040
- [16] Wukitch S.J. et al 2009 *J. Nucl. Mater.* **390–391** 951
- [17] Tuccillo A.A. et al 2009 *Nucl. Fusion* **49** 104013
- [18] Guilhem D. et al 2011 *Fusion Eng. Des.* **86** 279–87
- [19] Bibet Ph. et al 2000 *Fusion Eng. Des.* **51–52** 741–6
- [20] Delpech L. et al 2014 *Nucl. Fusion* **54** 103004
- [21] Dumont R.J. et al 2014 *Plasma Phys. Control. Fusion* **56** 075020
- [22] Goniche M. et al 2014 *Phys. Plasmas* **21** 061515
- [23] Ekedahl A. et al 2009 *Plasma Phys. Control. Fusion* **51** 044001
- [24] Ekedahl A. et al 2010 *Nucl. Fusion* **50** 112002
- [25] Decker J. et al 2011 *Nucl. Fusion* **51** 073025
- [26] Peysson Y. and Decker J. 2008 *Phys. Plasmas* **15** 092509
- [27] Cesario R. et al 2010 *Nature Commun.* **1** 55
- [28] Goniche M. et al 2013 *Nucl. Fusion* **53** 033010
- [29] Wallace G.M. et al 2010 *Phys. Plasmas* **17** 082508
- [30] Liu Z.X. et al 2012 *Plasma Phys. Control. Fusion* **54** 085005
- [31] Hoang G.T. et al 2009 *Nucl. Fusion* **49** 075001
- [32] Vulliez K. et al 2008 *Nucl. Fusion* **48** 065007
- [33] Argouarch A. et al 2009 *Fusion Eng. Des.* **84** 275–8
- [34] Colas L. et al 2006 *Nucl. Fusion* **46** S500
- [35] Bufferand H. et al 2013 *J. Nucl. Mater.* **438** S445
- [36] Dux R. et al 2003 *Plasma Phys. Control. Fusion* **45** 1815–25
- [37] Lerche E. et al 2014 ICRH for mitigation of core impurity accumulation in JET-ILW 25th IAEA Int. Conf. on Fusion Energy (St Petersburg, Russia, 2014) EX/PS-22 www.sciencedirect.com/science/article/pii/S0920379609000507
- [38] Basiuk V. et al 2004 *Nucl. Fusion* **44** 181
- [39] Dumont R.J. and Zaroso D. 2013 *Nucl. Fusion* **53** 013002
- [40] Eriksson L.-G. et al 2001 *Nucl. Fusion* **41** 91
- [41] Stix T.H. 1975 *Nucl. Fusion* **15** 737
- [42] Colas L. 2012 *Phys. Plasmas* **19** 092505
- [43] Schneider M. et al 2005 *Plasma Phys. Control. Fusion* **47** 2087–2106
- [44] Reux C. et al 2010 *Nucl. Fusion* **50** 095006
- [45] Saint Laurent F. et al 2013 *Fusion Sci. Technol.* **64** 711–18 www.ans.org/pubs/journals/fst/a_24090
- [46] Reiter D., Baelmans M. and Boerner P. 2005 *Fusion Sci. Technol.* **47** 172–86 www.ans.org/pubs/journals/fst/a_698
- [47] Martin Y.R. et al 2008 *J. Phys.: Conf. Ser.* **123** 012033
- [48] Takizuka T. et al 2004 *Plasma Phys. Control. Fusion* **46** A227–33
- [49] Maggi C.F. et al 2014 41st EPS Conf. on Plasma Physics (Berlin, Germany, 2014) <http://ocs.ciemat.es/EPS2014PAP/pdf/P1.004.pdf>
- [50] Minardi E.J. et al. 1997 *Plasma Phys.* **57** 449
- [51] Meyer O. et al 2013 40th EPS Conf. on Plasma Physics (Espoo, Finland, 2013) <http://ocs.ciemat.es/EPS2013PAP/pdf/P1.117.pdf>
- [52] Andrew Y. et al 2008 *Plasma Phys. Control. Fusion* **50** 124053
- [53] Tobita K. et al 1995 *Nucl. Fusion* **35** 1585
- [54] Gohil P. et al 2011 *Nucl. Fusion* **51** 103020
- [55] McDonald D.C. et al 2007 *Nucl. Fusion* **47** 147–74
- [56] Huysmans G.T.A. 2007 *Nucl. Fusion* **47** 659
- [57] Loarte A. et al 2003 *Plasma Phys. Control. Fusion* **45** 1549–69
- [58] Zaroso D. et al 2011 *Nucl. Fusion* **51** 112001
- [59] Herrmann A. 2002 *Plasma Phys. Control. Fusion* **44** 883
- [60] Huysmans G. et al 2009 *Plasma Phys. Control. Fusion* **51** 124012
- [61] Stangeby P. *The Plasma Boundary of Magnetic Fusion Devices (Series in Plasma Physics vol 7)* ed P. Stangeby (London: Taylor and Francis) [http://physics.technion.ac.il/~plasma/publications/ebooks/books2/djvu_library/Plasma/MHD%20abd%20Fusion/Stangeby%20P.%20The%20Plasma%20Boundary%20of%20Magnetic%20Fusion%20Devices%20\(ISBN%200750305592\)\(IoP,%202000\)\(715s\).pdf](http://physics.technion.ac.il/~plasma/publications/ebooks/books2/djvu_library/Plasma/MHD%20abd%20Fusion/Stangeby%20P.%20The%20Plasma%20Boundary%20of%20Magnetic%20Fusion%20Devices%20(ISBN%200750305592)(IoP,%202000)(715s).pdf)
- [62] Dux R. et al 2009 *J. Nucl. Mater.* **390–391** 858–63
- [63] Marandet Y. et al 2014 *Contrib. Plasma Phys.* **54** 353–7
- [64] Beurskens M. et al 2014 *Nucl. Fusion* **54** 043001
- [65] Kallenbach A. et al 2011 *Nucl. Fusion* **51** 094012
- [66] Kallenbach A. et al 2005 *J. Nucl. Mater.* **337–339** 381–5
- [67] Angioni C. et al 2007 *Nucl. Fusion* **47** 1326–35
- [68] Weisen H. et al 2005 *Nucl. Fusion* **45** L1
- [69] Staebler G. et al 2007 *Phys. Plasmas* **14** 055909
- [70] Bourdelle C. et al 2007 *Phys. Plasmas* **14** 112501
- [71] Artaud J.-F. et al 2010 *Nucl. Fusion* **50** 043001
- [72] Hoang G.T. et al 2003 *Phys. Rev. Lett.* **90** 155002
- [73] Angioni C. et al 2012 *Nucl. Fusion* **52** 114003
- [74] Bucalossi J. et al 2011 *Fusion Eng. Des.* **86** 684–8
- [75] Zagórski R. et al 2009 *J. Nucl. Mater.* **390** 404
- [76] Zagórski R. et al 2012 *Contrib. Plasma Phys.* **52** 379
- [77] Ivanov-Stanik I. et al 2013 IAEA Technical Meeting on Steady State Operation (Aix-en-Provence, France, 14–17 May 2013) www.naweb.iaea.org/naweb/physics/meetings/TM44767.html
- [78] Lipschultz B. et al 2001 *Nucl. Fusion* **41** 585
- [79] Bufferand H. et al 2014 *Contrib. Plasma Phys.* **54** 378
- [80] Marandet Y. et al 2015 *J. Nucl. Mater.* in press <http://dx.doi.org/10.1016/j.jnucmat.2014.11.030>
- [81] Marandet Y. et al 2011 *Nucl. Fusion* **51** 083035
- [82] Mekkaoui A. et al 2012 *Phys. Plasma* **19** 122310

- [83] Guzman-Fulgencio F. *et al* 2015 *J. Nucl. Mater.* in press
- [84] Chankin A. *et al* 2014 *Plasma Phys. Control. Fusion* **56** 025003
- [85] Ochoukov R. *et al* 2014 *Plasma Phys. Control. Fusion* **56** 015004
- [86] Colas L. *et al* 2015 *J. Nucl. Mater.* in press
<http://dx.doi.org/10.1016/j.jnucmat.2014.10.011>
- [87] Wukitch S. *et al* 2013 *Phys. Plasmas* **20** 056117
- [88] Kubic M. *et al* 2013 *J. Nucl. Mater.* **438** S509–12
- [89] Cziegler I. *et al* 2012 *Plasma Phys. Control. Fusion* **54** 105019
- [90] Ritz G. *et al* 2013 *Fusion Eng. Des.* **88** 899–902
- [91] Corre Y. *et al* 2011 *Fusion Eng. Des.* **86** 429–41
- [92] Jacquot J. *et al* 2014 *Phys. Plasmas* **21** 061509
- [93] ITER Physics Basis Expert Groups on Confinement and Transport and Confinement Modelling and Database, ITER Physics Basis Editors 1999 *Nucl. Fusion* **39** 2175
- [94] Pütterich T. *et al* 2010 *Nucl. Fusion* **50** 025012
- [95] Mahdavi M.A. *et al* 2003 *Phys. Plasmas* **10** 3984–91